remote sensing

MDPI

Article

A Comparative Study of the Landfall Precipitation by Tropical Cyclones ARB 01 (2002) and Luban (2018) near the Arabian Peninsula

Yusheng Cui [1,2], Haibin Lü [1,3,4,*], Dawei Shi [2], Chuqi Xia [1,2] and Changming Dong [5]

[1] Jiangsu Key Laboratory of Marine Bioresources and Environment, Jiangsu Key Laboratory of Marine Biotechnology, Jiangsu Ocean University, Lianyungang 222005, China; 2019220200@jou.edu.cn (Y.C.); 2020220434@jou.edu.cn (C.X.)
[2] Lianyungang Meteorological Bureau, Lianyungang 222005, China; lygsdw@163.com
[3] Co-Innovation Center of Jiangsu Marine Bio-Industry Technology, Jiangsu Ocean University, Lianyungang 222005, China
[4] Jiangsu Institute of Marine Resources Development, Lianyungang 222005, China
[5] School of Marine Sciences, Nanjing University of Information Science and Technology, Nanjing 210044, China; cmdong@nuist.edu.cn
* Correspondence: haibin_lv@jou.edu.cn

Abstract: Considering the high risk of flooding during tropical cyclones (TCs), there is great practical significance in researching and predicting precipitation during TC landfalls. Using NECP FNL reanalysis data and GPM_MERGIR datasets, two TCs with similar trajectories, ARB 01 in 2002 and Luban in 2018, were analyzed. For ARB 01 and Luban, there are separate effects of wind shear at different heights on the development of vertical motion. Meridional wind shear affects the main deviation direction of vertical motion (downshear), while zonal wind shear mainly affects the deviation direction of vertical motion to the left or right of downshear. The divergent configuration of wind promotes the development of vertical motion. The influence of wind speed provided ideal conditions for ARB 01 to generate symmetric precipitation along its path when it made landfall. Additionally, more water vapor support was obtained from the southern Indian Ocean, which enabled ARB 01 to have a larger and broader average precipitation rate after landing.

Keywords: tropical cyclones; precipitation; extreme tropical cyclone precipitation; extreme precipitation; Arabian Sea

Citation: Cui, Y.; Lü, H.; Shi, D.; Xia, C.; Dong, C. A Comparative Study of the Landfall Precipitation by Tropical Cyclones ARB 01 (2002) and Luban (2018) near the Arabian Peninsula. *Remote Sens.* **2022**, *14*, 1194. https://doi.org/10.3390/rs14051194

Academic Editor: Francisco J. Tapiador

Received: 15 January 2022
Accepted: 25 February 2022
Published: 28 February 2022

1. Introduction

Tropical cyclones (TCs) are often accompanied by extreme rainfall events when they make landfall, which may trigger flooding. TCs are one of the most destructive natural disasters in coastal regions of the world [1–3]. To better participate in emergency preparedness and reduce the impact of disasters, TC-related forecasting is particularly important. Although there has been significant progress in TC path predictions, there is still a large deficiency in precipitation predictions, and this is due largely to the inability to accurately predict rainfall distributions and intensities, thus leading to unexpected and often catastrophic disasters [4]. The total rainfall of a TC in the region depends greatly on the area covered by rainfall and the translational speed of the storm [5]. TC rainfall distributions are related to a variety of variables that include, but are not limited to, storm intensity, translational velocity, cyclone location, vertical wind shear (VWS), and large-scale environmental conditions [6–9]. TC landfall rainfall is also affected by the interaction of meteorological systems, which may lead to different rainfall distributions at seemingly similar landing sites [10]. In all ocean basins, the asymmetry of precipitation is usually determined by the motion of VWS and the TC over the sea surface, where the maximum precipitation occurs mainly downshear and to the left side of the environmental shear vector [11,12]. Before a

TC makes landfall, the maximum value of precipitation usually shifts to the front quadrant with respect to its movement direction. After landfall, the maximum precipitation often moves clockwise from the front right quadrant to the rear right quadrant, which can be caused by the combined effect of land interaction, TC movement, and VWS [13].

The north Arabian Sea is a semi-enclosed sea with a distinct monsoon climate, and TCs that usually bring heavy rainfall. TCs usually occur in May and June, associated with the southwest monsoon, and in November, associated with high sea level pressure in the Bay of Bengal [14]. As compared with the Bay of Bengal, less attention has been given to the precipitation of TCs in the Arabian Sea because of their lower frequency. TCs that make landfall on the Arabian Peninsula are particularly rare, but several strong ones have brought disasters to the peninsula in recent decades [15]. For example, TC Gonu in 2007 crossed the easternmost Ras Al Hadd of Oman with winds of 164 km/h on 5 June, bringing torrential rains of up to 610 mm near the eastern coastline, causing severe flooding damage [16]. TC Phet made landfall near Al Ashkharah in eastern Oman on 3 June 2010, and triggered torrential rains to wreak havoc on the area [17]. TC Chapala made landfall near Al Mukalla on Yemen's central coast on 3 November 2015, causing terrible rainfall and secondary disasters [18]. Studies show that the frequency of extremely intense cyclonic storms in the Arabian Sea is increasing [19], but there are few studies on the precipitation of landfall cyclones in the Arabian Peninsula. Therefore, it is of theoretical and practical significance to study TC precipitation (especially landfall precipitation) in the Arabian Sea. In this paper, the precipitation intensity and distribution of two TCs landing with similar tracks on the Arabian Peninsula were analyzed. Table 1 shows the cases of TCs used to study landfall precipitation, which lists the time, positions, intensities, and central pressure of their formation, landing, and disappearance.

Table 1. TC status, time, position, intensity, central pressure, and maximum wind speed is (MWS).

TC	Status	Date (DD/MM/YYYY)	Latitude (°N)	Longitude (°E)	MWS ($m \cdot s^{-1}$)	Central Pressure (hPa)
2002_ARB01	Generated	5 May 2002	8.6	67.7	25	1002
	Landfall	10 May 2002	16.5	53.3	32	997
	Dissipated	10 May 2002	17.4	53.1	30	1000
LUBAN	Generated	5 October 2018	11.2	68.9	20	1004
	Landfall	14 October 2018	15.8	52.2	35	996
	Dissipated	14 October 2018	16.5	51	25	1004

A comparative study of TC precipitation caused by ARB 01 in 2002 and Luban in 2018 was performed. The data and methodology are described in Section 2. The results are presented in Section 3, and discussion analyses are presented in Section 4. Finally, the conclusion is described in Section 5.

2. Data and Methodology

2.1. Data

The tracks of TCs ARB 01 and Luban were obtained from the Joint Typhoon Warning Center (JTWC; https://www.metoc.navy.mil/jtwc/jtwc.html accessed on 20 October 2021), which provided typhoon forecasts for the Western Pacific and Indian Ocean basins. Data of TC was at 6-hour intervals, including time, wind speed, and central location. The moving speed of a TC can be calculated according to the moving distance of the TC center every 6 h. The tracks of the two TCs are shown in Figure 1. As shown there, the path of 2002 ARB 01 is similar to that of 2018 Cyclone Luban, where 2002 ARB 01 was generated at 18:00 on 5 May 2002, landed at 12:00 on 10 May 2002, and dissipated at 18:00 on 10 May 2002. TC Luban was generated at 18:00 on 5 October 2018, landed at 06:00 on 14 October 2018, and dissipated at 18:00 on 14 October 2018. Both TCs had similar central pressures at landfall, but TC Luban's maximum wind speed was slightly stronger than that of ARB 01.

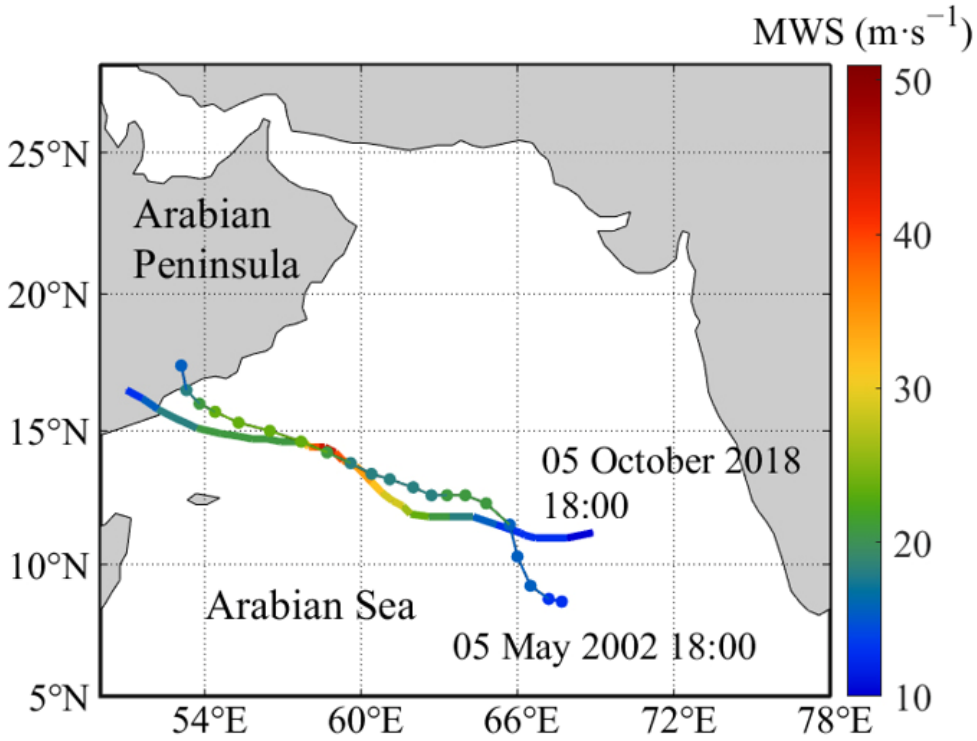

Figure 1. Paths and MWS (m·s^{-1}) of tropical cyclones ARB 01 and Luban. ARB 01 is represented by dots and Luban by lines.

The 0.5 h (0.1° × 0.1°) accumulated precipitation product was derived from GPM IMERG Final Precipitation (GPM_3IMERGHH). The GPM extends the TRMM sensor load and significantly improves its precipitation observation capability. Research has shown that IMERG products are far superior to ERA-Interim (European Centre for Medium Range Weather Forecasts) and TPMA-3B42 (TRMM and Multi-satellite Precipitation Analysis) products [20,21]. Data are available at https://disc.gsfc.nasa.gov/datasets/GPM_3IMERGHH_06/summary?keywords=%22IMERG%20final%22/ (accessed on 2 November 2021).

The GPM_MERGIR brightness temperature data with 0.5 h (4 km pixel resolution) (equivalent blackbody temperature) originate from NOAA/NCEP. Products come from European, Japanese, and American geostationary satellites (GOES-8/9/10/11/12/13/14/15/16, METEOSAT-5/7/8/9/10, and GMS-5/MTSat-1R/2/Himawari-8). The dataset has been widely used in scientific research [22]. Data are available at https://disc.gsfc.nasa.gov/datasets/GPM_MERGIR_1/summary/ (accessed on 5 November 2021).

NCEP FNL Operational Global Analysis data from the Global Data Assimilation System (GDAS) are used to obtain horizontal wind, vertical velocity, relative humidity, and air temperature. The data are available on temporal resolution of 6 h and the spatial resolution is (5/2)° × (5/2)°. Data are available at https://rda.ucar.edu/datasets/ds083.2/#description (accessed on 7 November 2021).

2.2. Methodology

The deep-level environmental vertical wind shear (EVWS) is usually defined as the difference of wind between 850 hPa and 200 hPa [9,23,24]. EVWS can be calculated according to Equations (1)–(3):

$$\overline{\Delta u}_{200-850} = \frac{\sum_1^n (u_{200i} - u_{850i})}{n} \quad (1)$$

$$\overline{\Delta v}_{200-850} = \frac{\sum_1^n (v_{200i} - v_{850i})}{n} \quad (2)$$

$$VWS = \left(\overline{\Delta u}_{200-850}\right) \cdot \vec{l} + \left(\overline{\Delta v}_{200-850}\right) \cdot \vec{J} \quad (3)$$

where u_{200} and u_{850} are the zonal wind speed at 200 hPa and 850 hPa, respectively. v_{200} and v_{850} are the meridional wind speed at 200 hPa and 850 hPa, respectively. *VWS* is the calculated environmental *VWS* vector. The low-level environmental *VWS* is usually the difference of wind between 700 hPa and 925 hPa, the calculation method is the same as deep-level environmental *VWS*. This method is also very mature in its usage [12,25,26].

The water vapor flux (*WVF*) is the amount of water vapor flowing through a unit area in unit time. *WVF* can be calculated according to Equation (4):

$$|WVF| = |\mathbf{V}|q/g \quad (4)$$

where v and q are the wind speed and specific humidity, respectively. g is the acceleration caused by gravity. This method is also very mature in its usage [27].

3. Results

3.1. Precipitation Distribution

The precipitation caused by a TC can be divided into inner core precipitation and outer rainband precipitation, where the total precipitation radius is often 300 km~500 km [28–30]. In this paper, the average and maximum precipitation rates in a region 400 km from the TC center are calculated to study the precipitation difference between ARB 01 and Luban.

Figure 2 shows the surface precipitation rate distribution of ARB 01 and Luban during the period of TC landfall and half an hour after TC landfall. TC ARB 01 made landfall at 12:00 on May 10, and precipitation was symmetrically distributed on both sides of the path in the back quadrant of the TC center. After landfall, precipitation was concentrated on the right and front of the TC center. TC Luban landed at 06:00 on October 14, and precipitation was concentrated in the rear quadrant of the TC center. After landing, the precipitation peak was still concentrated in the coastal area of the back quadrant. Table 2 shows their average and maximum precipitation rates within a radius of 400 km. At the time of landfall, the average and maximum precipitations of ARB 01 were less than those of Luban. After landfall, precipitation of ARB 01 extended inland and took up a wider distribution range with greater than 3 mm/h than that of Luban, although there was concentrated heavy precipitation for Luban. The precipitation peak of ARB 01 was 17.05 mm/h, less than that of Luban's 35.49 mm/h, but the average precipitation of ARB 01 (0.0042 mm/h) was stronger than that of Luban (0.0015 mm/h) within a radius range of 400 km.

Table 2. Average precipitation rate and maximum precipitation rate in a radius range of 400 km of the TC central pressure.

Tropical Cyclone	Date and Time	Average Precipitation (mm/h)	Maximum Precipitation (mm/h)
ARB 01	10 May 2002 12:00	0.0077	34.07
	10 May 2002 18:00	0.0042	17.05
Luban	14 October 2018 06:00	0.0099	60.80
	14 October 2018 12:00	0.0015	35.49

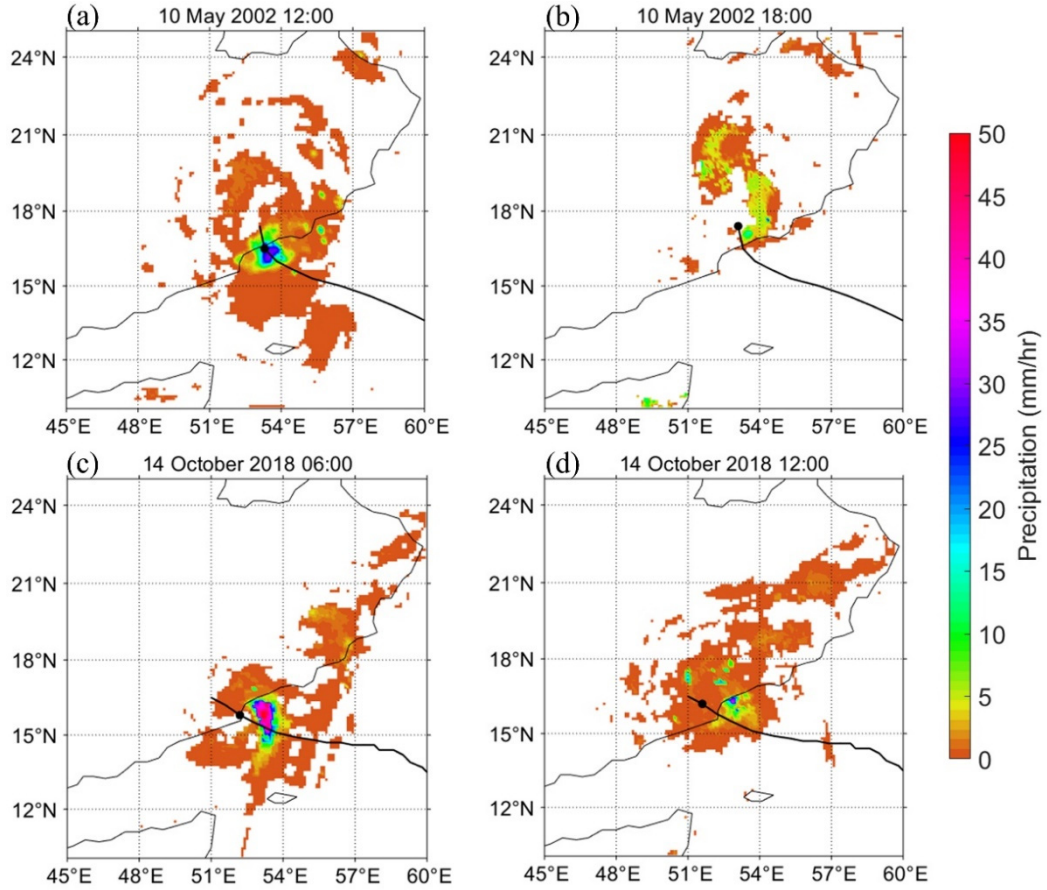

Figure 2. Precipitation (mm/h) distribution for ARB 01 on (**a**) 10 May 2002 12:00 and (**b**) 10 May 2002 18:00, and Luban on (**c**) 14 October 2018 06:00 and (**d**) 14 October 2018 12:00.

3.2. Brightness Temperature

As changes in the TC distribution of wind and precipitation can be studied using brightness temperature (BT), this and deep-level environmental VWS of the two TCs before, during, and after the TC made landfall are given in Figure 3. The lower the BT is, the higher the cloud top and the stronger the convection [31,32]. When BT is less than −75 °C, it is defined as the deep convection region [33]. Overall, the distribution in BT is essentially consistent with the precipitation in Figure 2. Before landfall, the VWS of ARB 01 and Luban were in the forward direction of the TC center, when the convection region appeared to the left of downshear. During landfall, the VWS direction of ARB 01 was in the direction of the TC, and the convection region appeared in the TC center and its right side, especially in the back quadrant of the TC center. BT was at the minimum at this position, and the deep convection region of −76.15 °C may be the main reason for the symmetrical distribution of precipitation. The VWS direction of the Luban rotated counterclockwise, which was opposite to the direction of the TC, where the convective region was to the left of the VWS. After landing, the VWS direction of ARB 01 was still in the positive quadrant of the TC direction, but the convection region was on the right side of the VWS. The direction of the VWS of Luban was in the opposite direction of the direction of TC, and the convection region was C-shaped surrounding the TC center, where the convection on the right side of downshear was stronger than that on the left. The low BT can reflect the spiral rainbands [34]. During and after the landfall of the TC, the spiral rainbands of ARB 01 were mainly distributed inland, and the spiral rainbands of Luban were mainly distributed along the coast. The distribution characteristics of the spiral rainbands are consistent with the precipitation distribution shown in Figure 2.

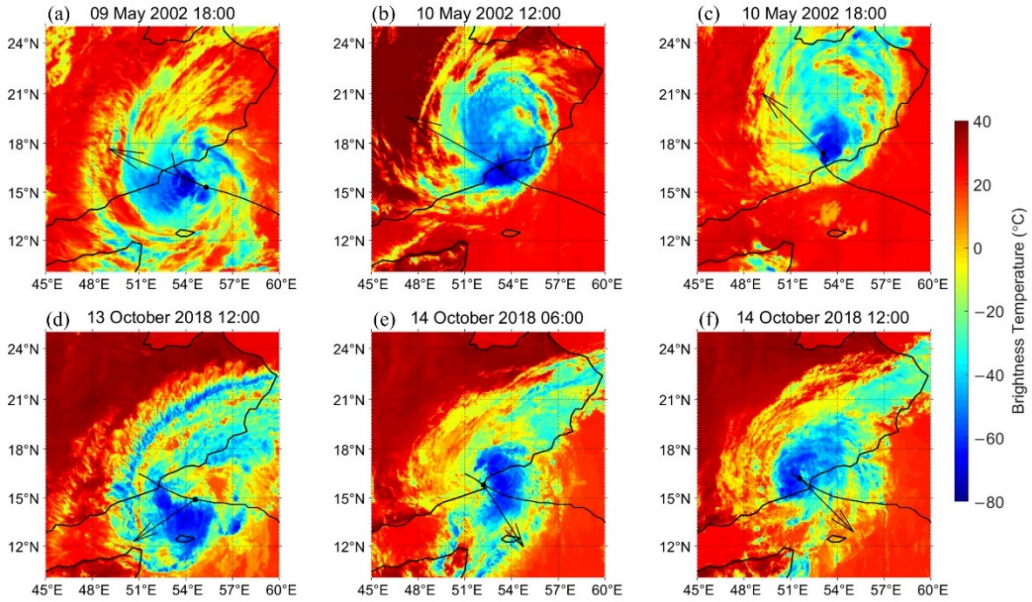

Figure 3. Brightness temperature (°C) distribution of ARB 01 on (**a**) 9 May 2002 18:00, (**b**) 10 May 2002 12:00, and (**c**) 10 May 2002 18:00, and Luban on (**d**) 13 October 2018 12:00, (**e**) 14 October 2018 06:00, and (**f**) 14 October 2018 12:00. The black arrow indicates the direction of the deep-level environment VWS.

3.3. Wind Speed

Yu et al. [35] calculated the estimated rainfall values of 133 landing TCs in China to test the relationship between TC intensity and rainfall distribution and found that the average rainfall rate and area of average rainfall were closely related to TC intensity, but there was no significant relationship between the maximum rainfall rate and TC intensity. Figure 4 shows the distribution of wind speed (WS) at 850 hPa of ARB 01 and Luban before, during, and after making landfall. From the correspondence between the WS and strong convection, it can be seen that wind intensity is also one of the reasons for determining the precipitation distribution in ARB 01 and Luban. The WS of ARB 01 was asymmetrical around the TC center before (Figure 4a), during (Figure 4b), and after landing (Figure 4c), but the WS was symmetric along the TC path at landing (Figure 4b). After the TC made landfall (Figure 4c), the WS was mainly concentrated on the right side of the TC path. The WS played an important supporting role in both symmetric precipitation on the TC path during landfall, and precipitation was mainly concentrated on the right side of the TC path after landfall. The Luban WS was symmetric about the TC center before landfall (Figure 4d), and asymmetric during (Figure 4e) and after landfall (Figure 4f), where the strong wind was concentrated on the right side of the TC path. Asymmetric WS plays an important role in supporting the asymmetric distribution of precipitation. In addition, it can be seen from Table 3 that the average wind speed of ARB 01 within the radius range of 400 km around the TC center was weaker than that of Luban, but the average wind speed of ARB 01 within the radius range of 400–1000 km around the TC center was stronger than that of Luban. After landing, ARB 01 was stronger than Luban in both carrying water vapor from the sea and invading the land interior, bringing more water vapor support for precipitation.

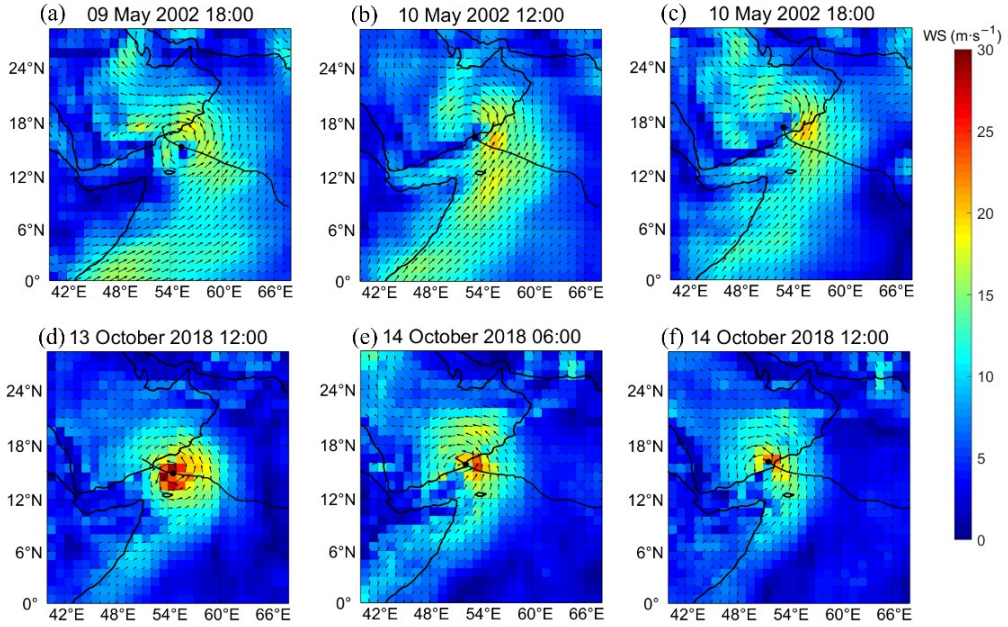

Figure 4. Wind speed (m/s) distribution of ARB 01 on (**a**) 9 May 2002 18:00, (**b**) 10 May 2002 12:00, and (**c**) 10 May 2002 18:00, and Luban on (**d**) 13 October 2018 12:00, (**e**) 14 October 2018 06:00, and (**f**) 14 October 2018 12:00. Black dots indicate the TC center.

Table 3. Average wind speed in a radius range of 400 km (400–1000 km) around the TC center.

Tropical Cyclone	Date and Time	Average Wind Speed in a Radius Range of 400 km around the TC Center (m/s)	Average Wind Speed in a Radius Range of 400–1000 km around the TC Center (m/s)
ARB 01	10 May 2002 12:00	12.7	10.2
	10 May 2002 18:00	11.6	9.7
Luban	14 October 2018 06:00	14.4	8.3
	14 October 2018 12:00	13.0	6.8

3.4. Water Vapor Flux

Figure 5 shows the WVF distribution of ARB 01 and Luban at 850 hPa during and after making landfall. WVF represents the water vapor source for TC precipitation. The water vapor sources of the two TCs are both from the sea surface and continuous water vapor transport from the southern Indian Ocean. Compared with Luban, ARB 01 has a tendency to carry more water vapor inland and has a stronger ability to transport water vapor from the sea after landfall. Figure 6 shows the variation of regional average water vapor flux of the two TCs with time series. Since 18 h before the TC's landing, the water vapor transported by ARB 01 had already exceeded Luban. After the TC's landing, the amount of water vapor transported between ARB 01 and Luban was further expanded, providing more water vapor and more sustained water vapor support for ARB 01's precipitation. More water vapor supports the regional average precipitation of ARB 01.

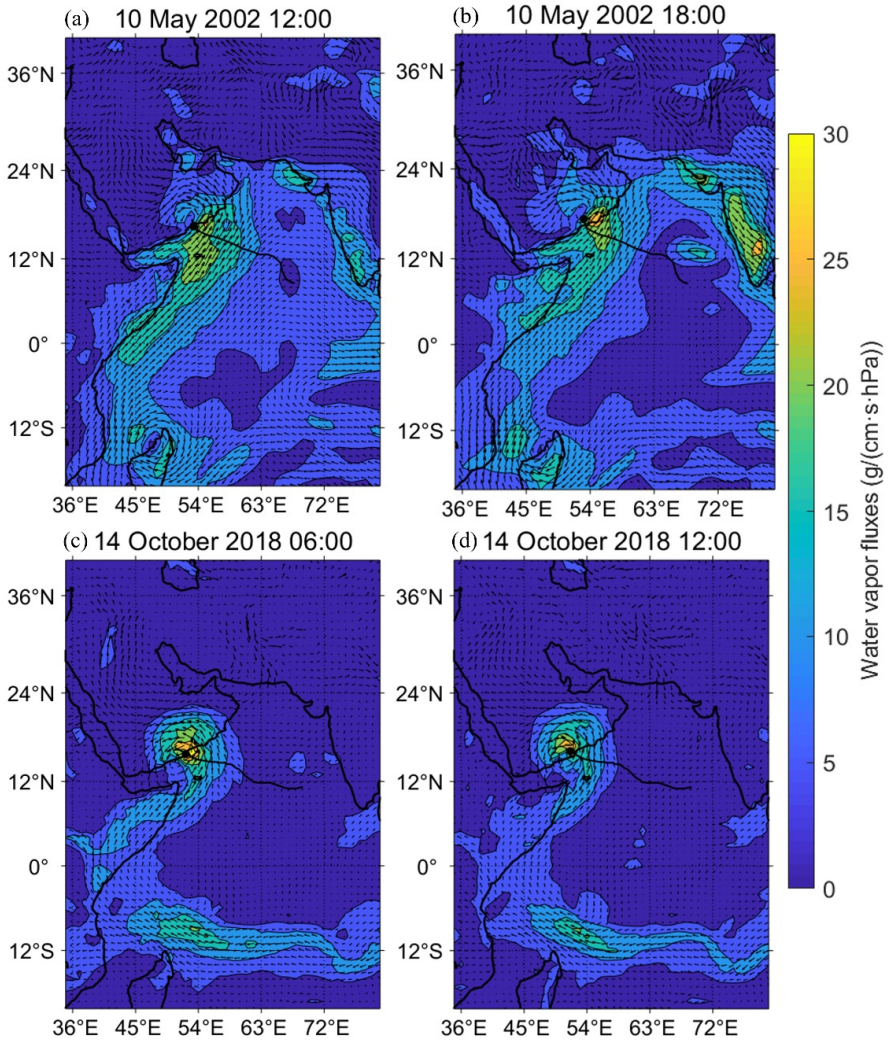

Figure 5. Water vapor fluxes distribution of ARB 01 on (**a**) 10 May 2002 12:00, and (**b**) 10 May 2002 18:00 at level = 850 hPa and Luban on (**c**) 14 October 2018 06:00, and (**d**) 14 October 2018 12:00 at level = 850 hPa. Black dots indicate the TC center.

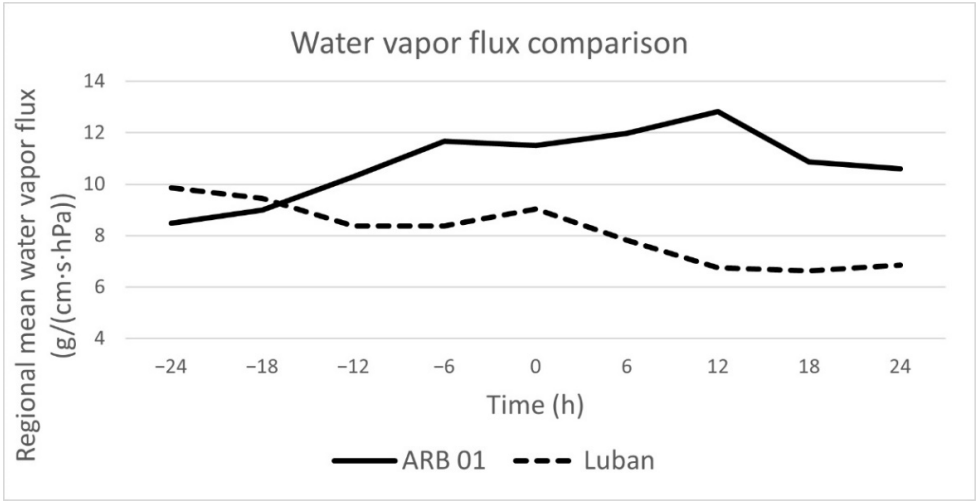

Figure 6. Regional (an area in a radius range of 1000 km centered on the landing site) average water vapor flux changes with time series.

4. Discussion

4.1. Vertical Wind Shear and Atmospheric Vertical Motion

Many scholars have studied the relationship between vertical shear and vertical motion of wind. For example, Frank and Ritchie [36] conducted a series of numerical simulations of TCs in an idealized large-scale environment and found that the maximum upward motion was continuously located on the left side of the downshear. Furthermore, Corbosiero and Molinari [37] proposed three mechanisms for vertical motion on the left side of downshear, namely the upper anticyclonic shear advection along the center of shear, the β effect, and the relationship between zonal wind and meridional potential vorticity. Generally, the maximum vertical movement is located to the left of the downshear, while heavy precipitation continues to move farther with the counterclockwise rotation of TC [38]. However, Finocchio et al. [24] conducted statistical analysis on environmental wind profiles of 7554 TC cases in the tropical Northern Hemisphere and found that VWS occurred in separate locations under different conditions, so both high and low levels may be affected by VWS. Demonstrating this, Figure 7 shows the variations in the 200–800 km mean meridional zonal wind at different levels.

In Figure 7a,b, it can be observed that shear mainly occurs at low levels below 600 hPa and high levels above 400 hPa. The low-level shear tends to the southeast direction, the high-level shear tends to the northwest direction, and the low-level shear is weaker than the high-level shear (Figure 7a). Combined with the observations in Figure 8a, it can be found that weak shear at a low level (low-level environment VWS has a value of 2.67 m/s) has difficulty preventing the development of vertical motion. Therefore, affected by high-level shear, vertical motion tends to be in the downshear of the deep-level environment VWS. Due to the strong upper-air north wind shear (Figure 7a), the vertical movement tends to the right of the downshear. In Figure 7b, the low-level (high-level) shear tends to the southeast (northwest), where the low-level shear is slightly weaker than the high-level shear. Combined with the observations in Figure 8b, it can be found that when the low-level shear is stronger, vertical movement is mainly controlled by the low-level shear (low-level environmental VWS has a value of 4.65 m/s), with the north wind shear and the preference for vertical movement along the left side of the downshear. In Figure 7c,d, shear mainly occurs at the low level below 600 hPa, the medium level between 400–600 hPa, and the high level above 200 hPa. The meridional and zonal winds are equal in magnitude and opposite in direction below 700 hPa. Therefore, the vertical movement below 700 hPa mainly occurred in the TC center (Figure 9a). In the rising process (Figure 7c), influenced by easterly shear, the vertical movement tended to downshear the deep-level VWS. As of the strong north wind shear in the middle layer, the vertical movement tends to the left side of the downshear. In Figure 7d, the shear changes from a low to a high level in a southeast direction. In the middle layer, the shear is influenced by weak north wind shear, so the vertical movement mainly tends to follow the shear direction of the deep-level environment VWS. In addition, the vertical movement on the south side of the shear is stronger than that on the north side, forming the C-shaped convection region in Figure 3f.

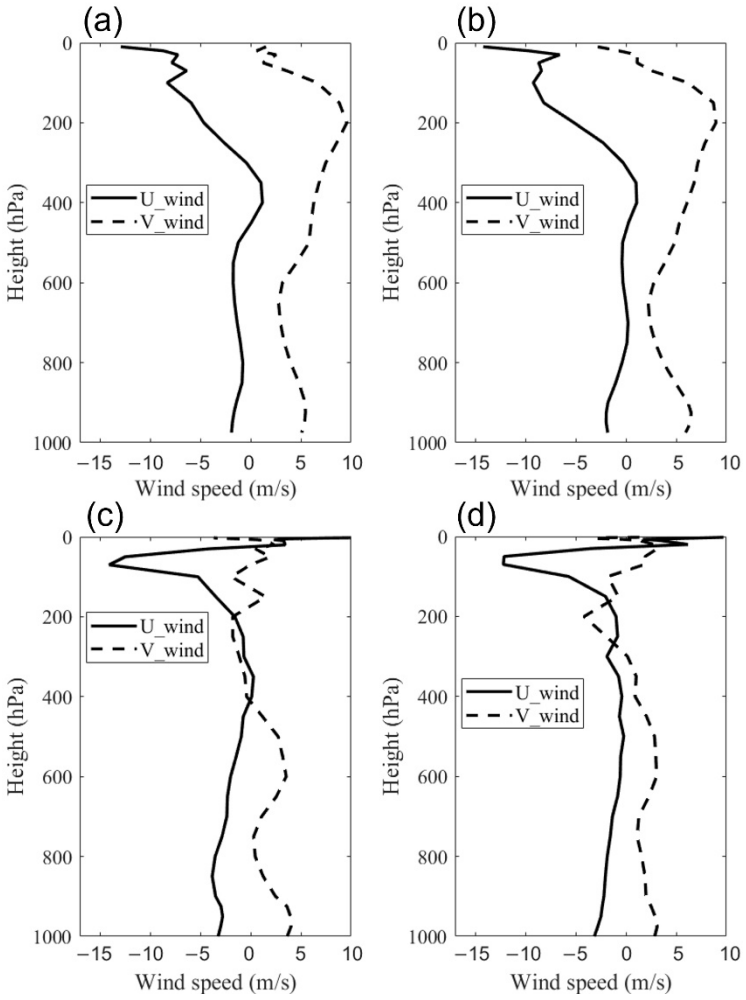

Figure 7. Variation in 200–800 km mean meridional (U_wind)(m/s) and zonal (V_wind)(m/s) winds at (**a**) 10:12, May 2002, (**b**) 10:18, May 2002, (**c**) 14:06, October 2018, and (**d**) 14:12, October 2018.

Summarizing, wind shear has an overall influence on the organization of vertical motion by the deep-level environment VWS and is further adjusted by mid-level shear. When mid-level shear is stronger, the vertical movement tends to the shear direction as a whole and then tends to the north side of the downshear under the influence of zonal wind (Figure 9a). When mid-level shear is weaker, the vertical motion in the middle layer tends to be slightly in the direction of zonal wind deflection (Figure 9b). When the zonal and meridional wind have a large difference in intensity, when low-level shear is stronger (weaker), vertical movement is mainly influenced by low-level (high-level) shear and vertical movement toward the direction of the low-level (deep-level) environment VWS in Figure 8b (Figure 8a). For ARB 01 and Luban, meridional wind shear mainly affects the deviation direction (downshear) of vertical motion, and zonal wind shear mainly affects the deviation direction of vertical motion to the left or right of the downshear.

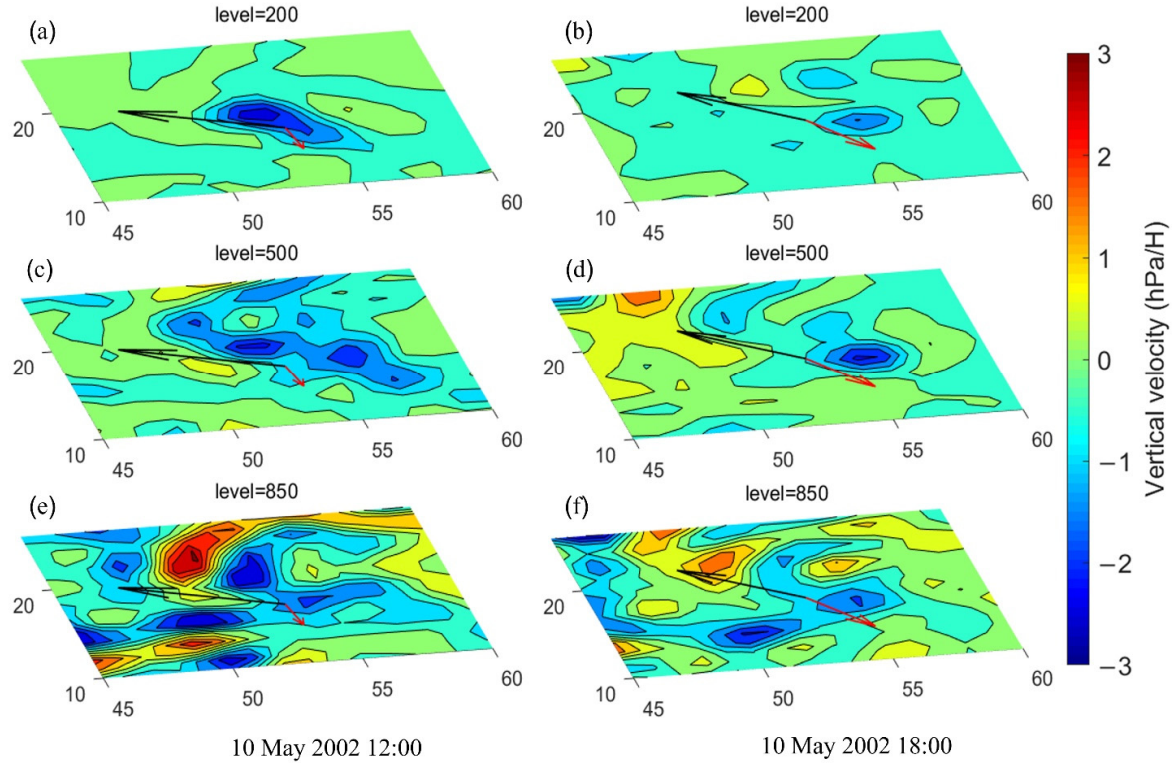

Figure 8. The vertical velocity (hPa/H) distribution of ARB 01 during (**a**,**c**,**e**) and after landfall (**b**,**d**,**f**) at level = 850 hPa, level = 500 hPa, and level = 200 hPa. The black arrow represents the deep-level environment VWS, and the red arrow represents the low-level environment VWS.

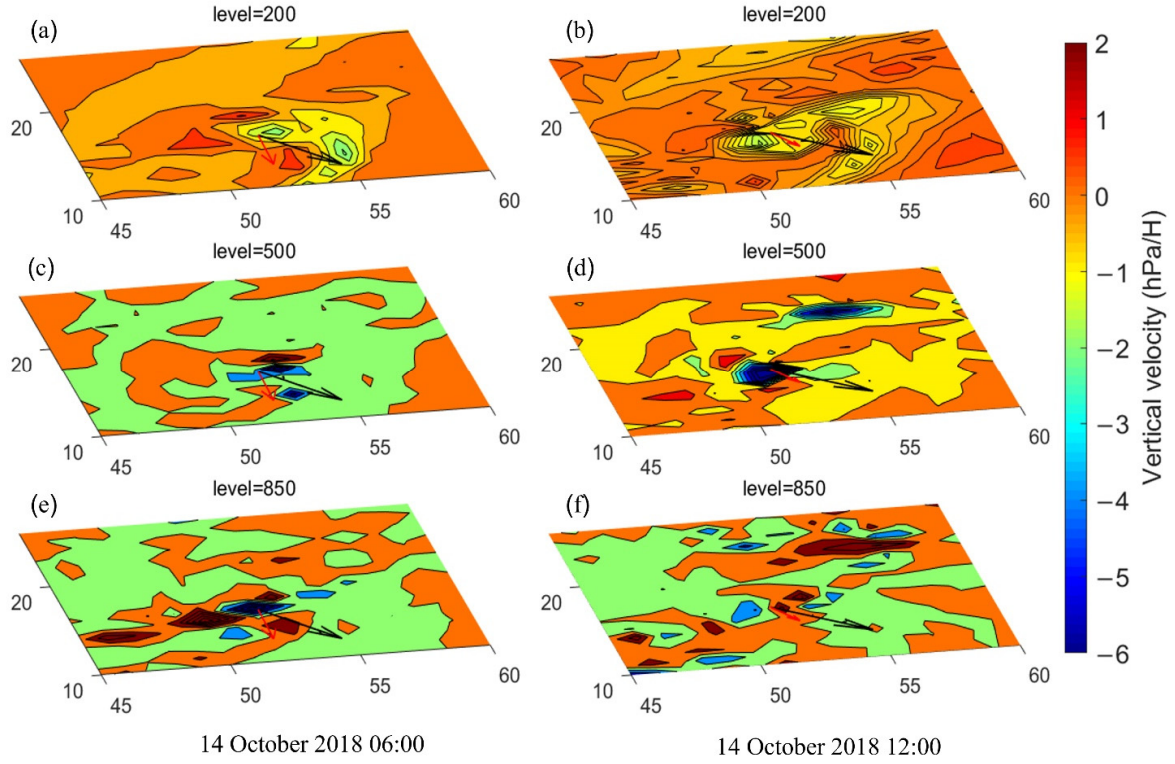

Figure 9. The vertical velocity (hPa/H) distribution of Luban during (**a**,**c**,**e**) and after landfall (**b**,**d**,**f**) at level = 850, level = 500, and level = 200. The black arrow represents the deep-level environment VWS, and the red arrow represents the low-level environment VWS.

4.2. Divergence Configuration

The configuration of convergence at a low level and divergence at a high level are conducive to the development of upward motion and the growth of strong convection [38,39]. Figures 10 and 11 show the divergence field distribution of ARB 01 and Luban at 850 hPa and 200 hPa. Negative (positive) values of divergence indicate convergence (divergence). During and after the landing of ARB 01, there was a strong divergence in the upper right part and convergence in the lower right part along the TC path, which promoted the upward movement on the right side of the TC path. Luban was also configured with low-level convergence and upper-level divergence during and after making landfall. During the landing period, upper-level divergence mainly occurred on the right side of the TC path (Figure 11a), while low-level convergence was almost symmetrical on both sides of the path (Figure 11c), with stronger convection on the right side of the TC path (Figure 3e). After making landfall, the low-level convergence zone is distributed on the left side of the TC path (Figure 11d), and the high-level divergence zone is distributed on both sides of the path (Figure 11b), resulting in the convection on the left side being stronger than that on the right (Figure 3f). Therefore, under the guidance of the atmospheric environment, convection is further strengthened.

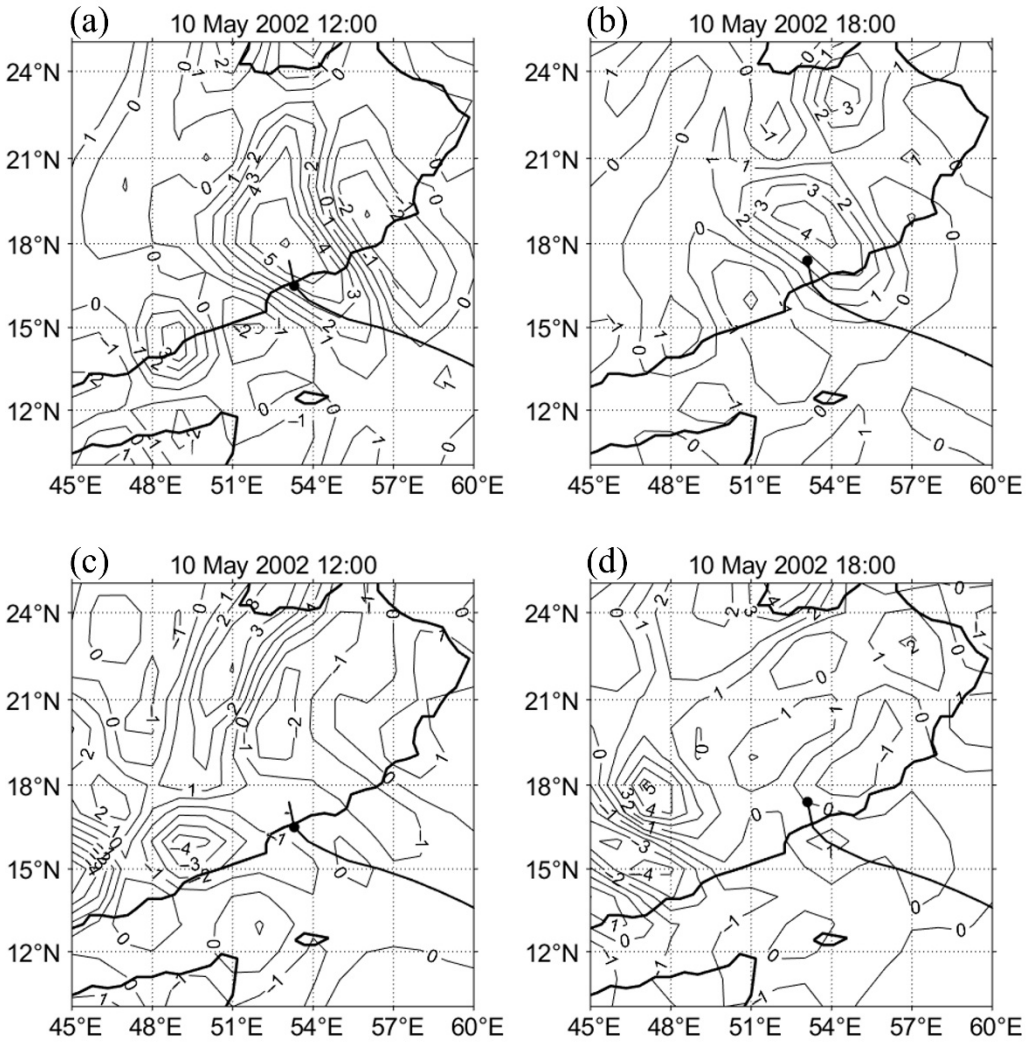

Figure 10. The divergence (10^{-5} s^{-1}) of ARB 01 during and after landfall. (**a**) 10 May 2002 12:00, (**b**) 10 May 2002 18:00 at level = 200 hPa; (**c**) 10 May 2002 12:00, (**d**) 10 May 2002 18:00 at level = 850 hPa. The black dot indicates the TC center.

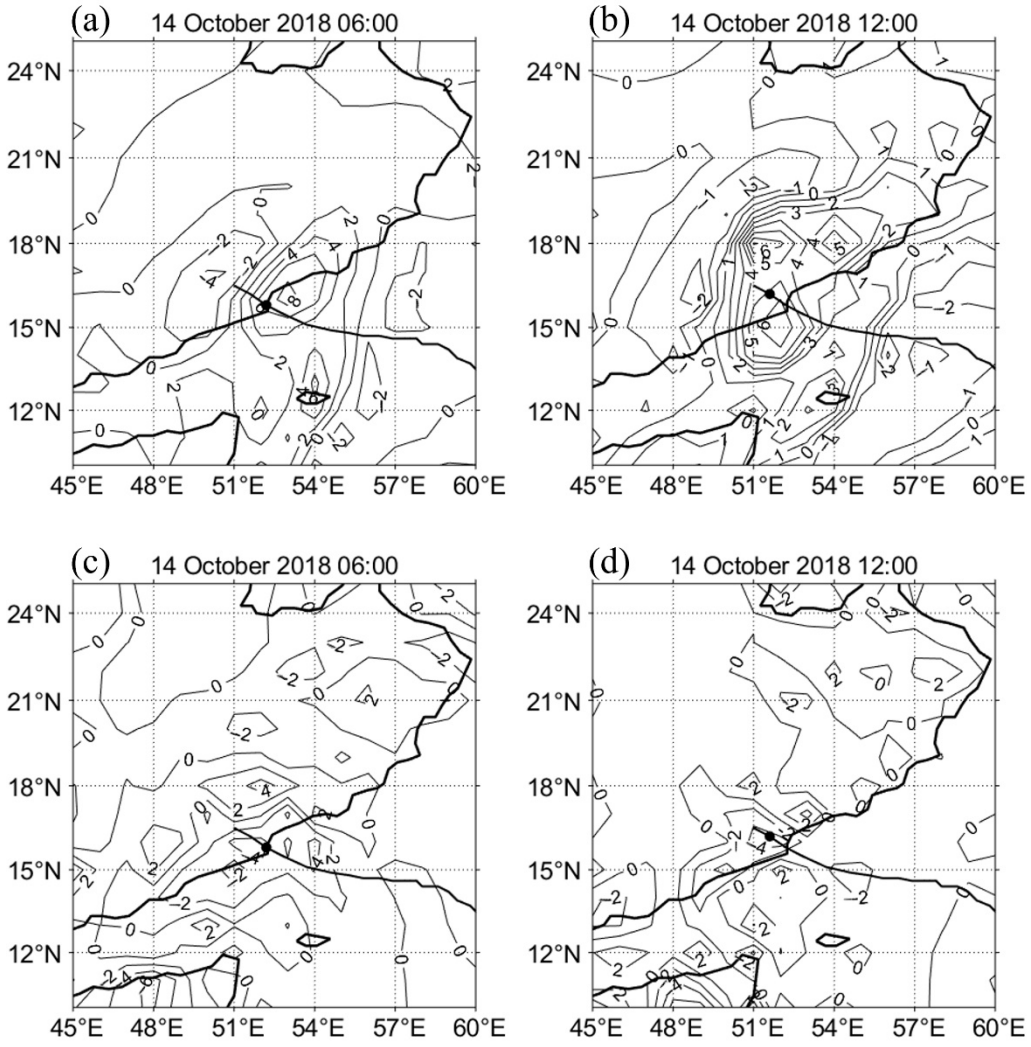

Figure 11. The divergence (10^{-5} s^{-1}) of Luban during and after landfall. (**a**) 14 October 2018 06:00, (**b**) 14 October 2018 12:00 at level = 200 hPa; (**c**) 14 October 2018 06:00, (**d**) 14 October 2018 12:00 at level = 850 hPa. The black dot indicates the TC center.

4.3. The Coordination of WVF and Vertical Velocity in Vertical Direction

Figure 12 shows the zonal profiles of WVF and vertical velocity during and after landfall for ARB 01 and Luban. Figure 13 shows the meridional profiles of WVF and vertical velocity during and after landfall for ARB 01 and Luban. For ARB 01, during landfall in the zonal direction (Figure 12a), ascending movement mainly occurred on the north side of the TC center with a maximum ascending velocity of −2.5 hPa/H and on the south side with a maximum ascending velocity of −1 hPa/H below 700 hPa. The WVF in the south is closer to the core of TC. In the north, although there is strong vertical movement in the spiral rain belt and less water vapor supply, the precipitation in the north is weaker than that in the south of the TC center. In the meridian direction (Figure 13a), water vapor is noticeably concentrated on the east side of the TC center due to the ocean providing more water vapor sources. After landfall, the WVF and vertical velocity are closely linked. In Figure 12b, the vertical velocity rising to a higher altitude is generally inclined to the north side of the TC center and carries a small amount of water vapor. In Figure 13b, both the vertical velocity and WVF are clearly concentrated on the east side of the TC center, so precipitation is concentrated on the east side of the TC center.

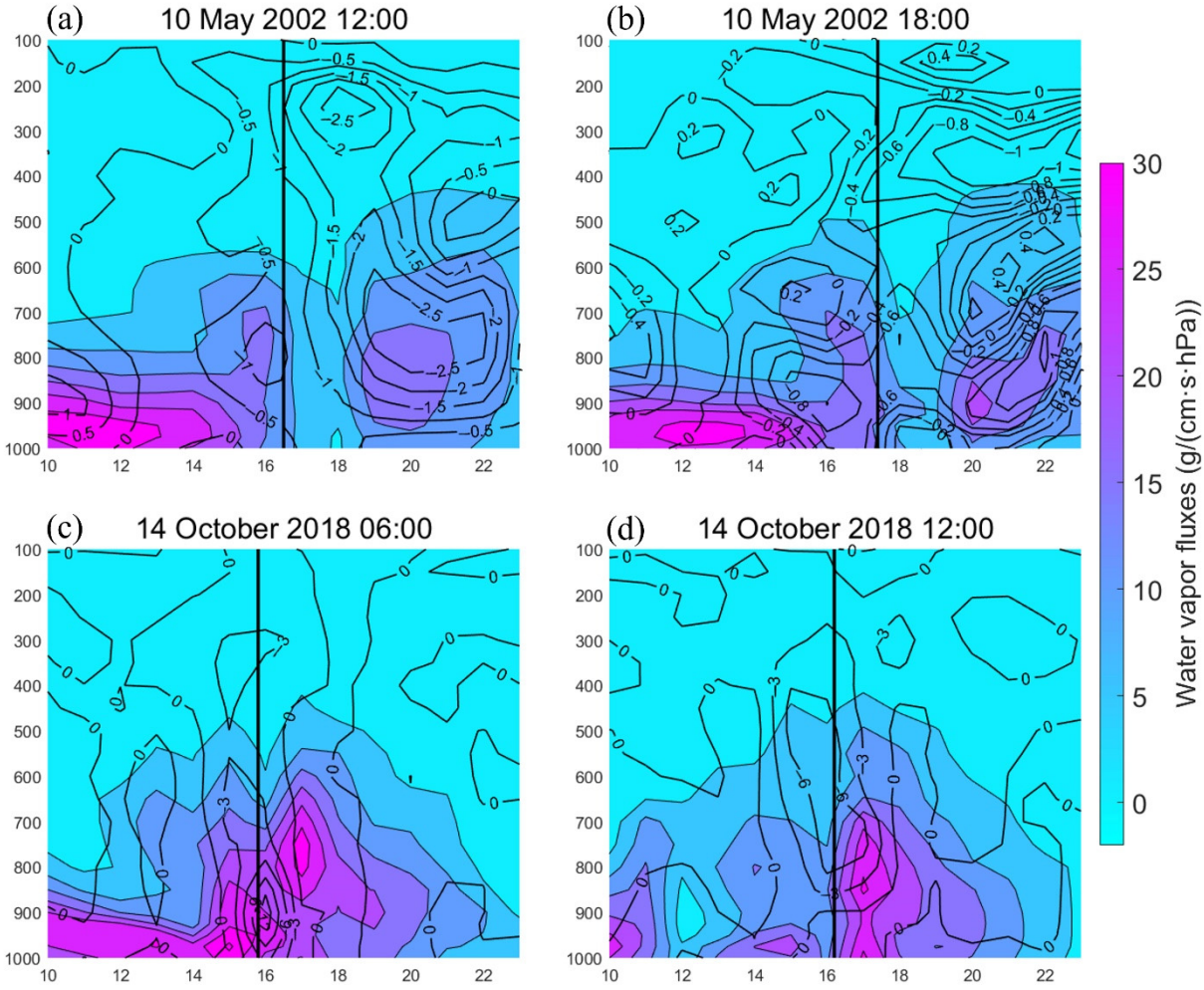

Figure 12. Zonal profiles of WVF and vertical velocity during and after landfall of ARB 01 (**a**,**b**) and Luban (**c**,**d**), where background colors indicate WVF. Black contour lines indicate vertical velocity.

For Luban, during landfall in the zonal direction (Figure 12c), the vertical movement of the atmosphere is close to the TC center, the rising height is insufficient, and the height is below 600 hPa. In the meridional direction (Figure 13c), the WVF is concentrated on the east side of the TC center near the ocean, and the vertical movement is offset between 600–800 hPa. After landfall, in the zonal direction (Figure 12d), the WVF tends to the north side of the TC center, but the vertical movement tends to the south side of the TC center from low to high. In the meridian direction (Figure 13d), the WVF on the east side of the TC center is noticeably stronger than that on the west side, but the vertical movement of water vapor on the west side of the TC center rises higher and then tends to the east side. The combination of vertical motion and poor WVF results in no heavy precipitation in the core.

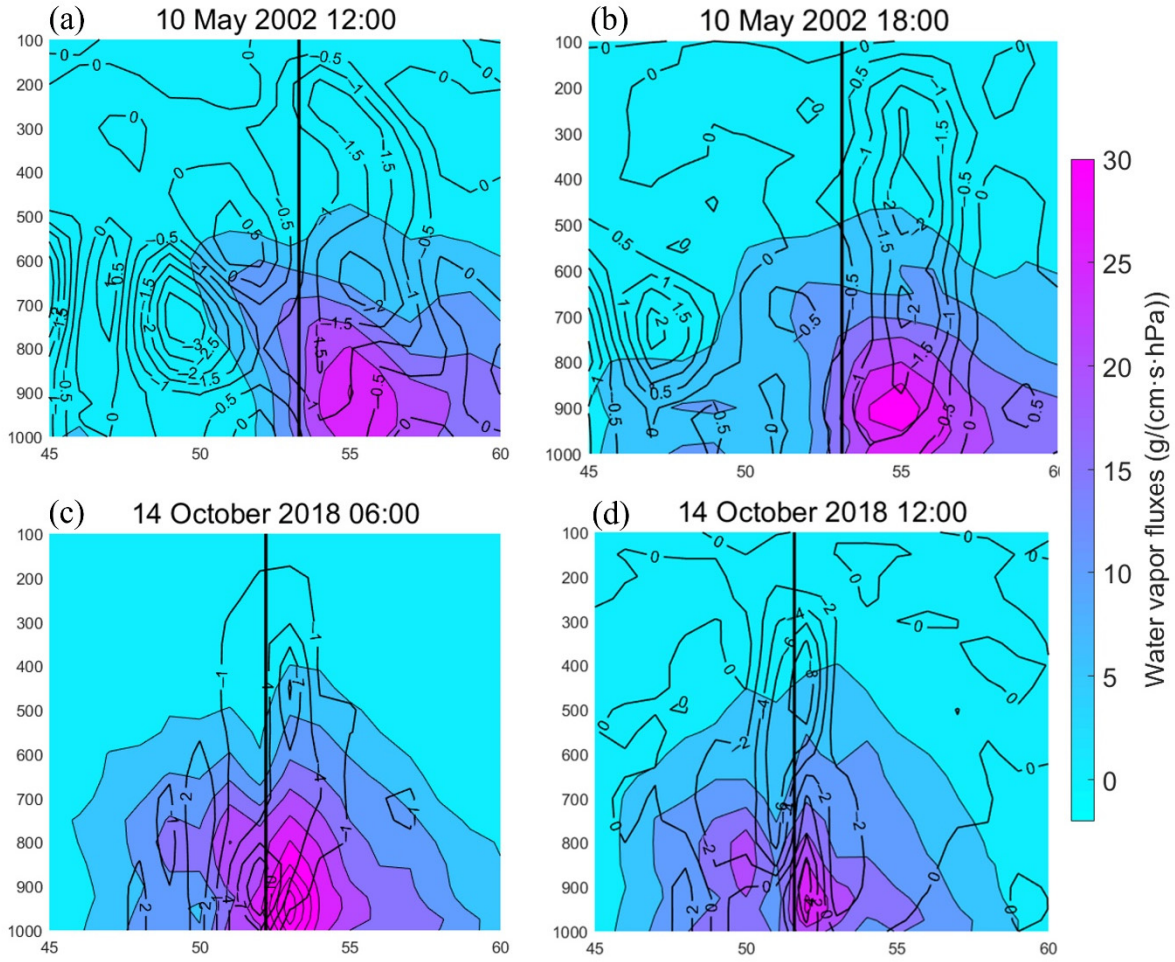

Figure 13. Meridional profiles of WVF and vertical velocity during and after landfall of ARB 01 on (**a**) 10 May 2002 12:00, (**b**) 10 May 2002 18:00, and Luban at landfall on (**c**) 14 October 2018 06:00, and (**d**) 14 October 2018 12:00.

5. Conclusions

The environmental VWS, BT, WS, and WVF and the divergence of TCs ARB 01 and Luban with same paths were analyzed to study the influence on precipitation distribution. It was identified that for ARB 01 and Luban, meridional wind shear affects the main deviation direction of vertical motion (downshear), while zonal wind shear mainly affects the deviation direction of vertical motion to the left or right of downshear. When ARB 01 made landfall, because of the influence of high-level wind shear, convection was mainly distributed on the right side of the shear of deep-level environment VWS. However, as there was not enough water vapor, heavy precipitation could not form on the right side of the shear. After landfall, convection with the influence of low-level shear mainly occurred on the right side of the downshear of low-level environment VWS. Luban was generally influenced by deep-level environment VWS and adjusted by wind shear in the middle layer. Additionally, it was shown that the divergence configuration of high-level and low-level divergence promoted the development of vertical movement, and further provided environmental support for precipitation distribution.

Precipitation requires abundant water vapor support in addition to vertical movement. Due to the lack of water vapor support, at the north side of the TC when ARB 01 landed and in the core of the TC after Luban landed, heavy precipitation could not be formed. Under the influence of the TC wind field, although the overall WS of the ARB 01 circulation was weaker than that of Luban, the WS of the peripheral flow field was stronger than that of Luban. Under this influence, more water vapor support can be obtained from the southern

Indian Ocean. After landing, the average precipitation rate of ARB 01 was stronger than that of Luban. At the time of landing, the WS of ARB 01 was approximately symmetric about the path, while the strong WS of Luban was biased to the right of the TC path. This is also one of the reasons why the precipitation of ARB 01 was symmetric about the TC path, while the precipitation of Luban was biased to the right of the TC path.

Author Contributions: Conceptualization, Y.C. and H.L.; methodology, Y.C. and H.L.; software, Y.C.; validation, Y.C., H.L., D.S., C.X. and C.D.; formal analysis, Y.C. and H.L.; investigation, Y.C. and D.S.; resources, Y.C. and H.L.; data curation, Y.C. and C.D.; writing—original draft preparation, Y.C. and H.L.; writing—review and editing, Y.C., H.L., D.S., C.X. and C.D.; visualization, Y.C. and C.X.; supervision, Y.C. and H.L.; project administration, Y.C. and H.L.; funding acquisition, Y.C., H.L. and C.X. All authors have read and agreed to the published version of the manuscript.

Funding: This work was funded by the Postgraduate Research & Practice Innovation Program of Jiangsu Province (Grant no. SJCX20_1246, SJCX21_1487), the Priority Academic Program Development of the Jiangsu Higher Education Institutions (PAPD), the Open Fund of the Jiangsu Institute of Marine Resources Development (Grant no. JSIMR202005), the East China regional meteorological science and technology collaborative innovation fund cooperation project (Grant no. qyhz201803), and the National Natural Science Foundation of China (Grants no. 62071207).

Data Availability Statement: Data can be available from the Joint Typhoon Warning Center (JTWC; https://www.metoc.navy.mil/jtwc/jtwc.html, accessed on 20 October 2021), GPM IMERG Final Precipitation (GPM_3IMERGHH; https://disc.gsfc.nasa.gov/datasets/GPM_3IMERGHH_06/summary?keywords=%22IMERG%20final%22/, accessed on 2 November 2021), GPM_MERGIR brightness temperature data from NOAA/NCEP (https://disc.gsfc.nasa.gov/datasets/GPM_MERGIR_1/summary/, accessed on 5 November 2021), NCEP FNL Operational Global Analysis data from the Global Data Assimilation System (GDAS; https://rda.ucar.edu/datasets/ds083.2/#description, accessed on 7 November 2021).

Acknowledgments: We thank the Joint Typhoon Warning Center (JTWC; https://www.metoc.navy.mil/jtwc/jtwc.html accessed on 20 October 2021), GPM IMERG Final Precipitation (GPM_3IMERGHH; https://disc.gsfc.nasa.gov/datasets/GPM_3IMERGHH_06/summary?keywords=%22IMERG%20final%22/ accessed on 2 November 2021), GPM_MERGIR brightness temperature data from NOAA/NCEP (https://disc.gsfc.nasa.gov/datasets/GPM_MERGIR_1/summary/ accessed on 5 November 2021), NCEP FNL Operational Global Analysis data from the Global Data Assimilation System (GDAS; https://rda.ucar.edu/datasets/ds083.2/#description accessed on 7 November 2021).

Conflicts of Interest: The authors declare no conflict of interest. The funders had no role in the design of the study, in the collection, analyses, or interpretation of data, in the writing of the manuscript, or in the decision to publish the results.

References

1. Guan, S.; Li, S.; Hou, Y.; Hu, P.; Liu, Z.; Feng, J. Increasing threat of landfalling typhoons in the western North Pacific between 1974 and 2013. *Int. J. Appl. Earth Observ. Geoinf.* **2018**, *68*, 279–286. [CrossRef]
2. Srisangeerthanan, S.; Lewangamage, C.S.; Wickramasuriya, S.S. Tropical Cyclone Damages in Sri Lanka. *Wind Eng. JAWE* **2015**, *40*, 294–302. [CrossRef]
3. Zhang, Q.; Wu, L.; Liu, Q. Tropical Cyclone Damages in China 1983–2006. *Bull. Am. Meteorol. Soc.* **2009**, *90*, 489–496. [CrossRef]
4. Yu, Z.; Wang, Y. *Rainfall Distribution in Landfalling Tropical Cyclones*; IntechOpen: London, UK, 2018. [CrossRef]
5. Rogers, R.; Marks, F.; Marchok, T. *Tropical Cyclone Rainfall*; John Wiley & Sons: Hoboken, NJ, USA, 2009. [CrossRef]
6. Chen, B.-F.; Davis, C.A.; Kuo, Y.-H. Examination of the Combined Effect of Deep-Layer Vertical Shear Direction and Lower-Tropospheric Mean Flow on Tropical Cyclone Intensity and Size Based on the ERA5 Reanalysis. *Mon. Weather Rev.* **2021**, *149*, 4057–4076. [CrossRef]
7. Matayas, C. Relating tropical cyclone rainfall patterns to storm size. In Proceedings of the Delivered at the Association of American Geographers South East Division Annual Meeting, West Palm Beach, FL, USA, 21 November 2005.
8. Rodgers, E.B.; Baik, J.-J.; Pierce, H.F. The Environmental Influence on Tropical Cyclone Precipitation. *J. Appl. Meteorol.* **1994**, *33*, 573–593. [CrossRef]
9. Shi, D.; Chen, G. The Implication of Outflow Structure for the Rapid Intensification of Tropical Cyclones under Vertical Wind Shear. *Mon. Weather Rev.* **2021**, *149*, 4107–4127. [CrossRef]
10. Titley, H.A.; Cloke, H.L.; Harrigan, S.; Pappenberger, F.; Prudhomme, C.; Robbins, J.C.; Stephens, E.M.; Zsoter, E. Key factors influencing the severity of fluvial flood hazard from tropical cyclones. *J. Hydrometeorol.* **2021**, *22*, 180–181. [CrossRef]

11. Chen, S.S.; Knaff, J.A.; Marks, F. Effects of Vertical Wind Shear and Storm Motion on Tropical Cyclone Rainfall Asymmetries Deduced from TRMM. *Mon. Weather Rev.* **2006**, *134*, 3190–3208. [CrossRef]
12. Wingo, M.T.; Cecil, D.J. Effects of Vertical Wind Shear on Tropical Cyclone Precipitation. *Mon. Weather Rev.* **2010**, *138*, 645–662. [CrossRef]
13. Wu, D.; Zhao, K.; Jou, B.J.-D.; Lee, W.-C. Radar Observation of Precipitation Asymmetries in Tropical Cyclones Making Landfall on East China Coast. *Trop. Cyclone Res. Rev.* **2013**, *2*, 81–95. [CrossRef]
14. Evan, A.T.; Camargo, S. A Climatology of Arabian Sea Cyclonic Storms. *J. Clim.* **2011**, *24*, 140–158. [CrossRef]
15. Terry, J.P.; Gienko, G. Quantitative observations on tropical cyclone tracks in the Arabian Sea. *Arch. Meteorol. Geophys. Bioclimatol. Ser. B* **2019**, *135*, 1413–1421. [CrossRef]
16. Fritz, H.M.; Blount, C.D.; Albusaidi, F.B.; Al-Harthy, A.H.M. Cyclone Gonu storm surge in Oman. *Estuar. Coast. Shelf Sci.* **2010**, *86*, 102–106. [CrossRef]
17. Haggag, M.; Badry, H. Hydrometeorological Modeling Study of Tropical Cyclone Phet in the Arabian Sea in 2010. *Atmosph. Clim. Sci.* **2012**, *02*, 174–190. [CrossRef]
18. Bhattacharya, S. Evolution of thErmodynamic structurEs during rapid growth and dEcay of ExtrEmEly sEvErE cyclonic storm Chapala. *Trop. Cyclone Res. Rev.* **2018**, *6*, 67–81. [CrossRef]
19. Murakami, H.; Vecchi, G.A.; Underwood, S. Increasing frequency of extremely severe cyclonic storms over the Arabian Sea. *Nat. Clim. Chang.* **2017**, *7*, 885–889. [CrossRef]
20. Sharifi, E.; Steinacker, R.; Saghafian, B. Assessment of GPM-IMERG and Other Precipitation Products against Gauge Data under Different Topographic and Climatic Conditions in Iran: Preliminary Results. *Remote Sens.* **2016**, *8*, 135. [CrossRef]
21. Kim, M.-J.; Jin, J.; El Akkraoui, A.; McCarty, W.; Todling, R.; Gu, W.; Gelaro, R. The Framework for Assimilating All-Sky GPM Microwave Imager Brightness Temperature Data in the NASA GEOS Data Assimilation System. *Mon. Weather Rev.* **2020**, *148*, 2433–2455. [CrossRef]
22. Nguyen, K.T.; Hu, L.; Alenin, A.S.; Ritchie, E.A.; Tyo, J.S. A Satellite-Based Remote-Sensing Framework to Quantify the Upwelling Radiation Due to Tropical Cyclones. *IEEE J. Sel. Top. Appl. Earth Obs. Remote Sens.* **2021**, *14*, 5488–5500. [CrossRef]
23. Yu, Z.; Wang, Y.; Xu, H. Observed Rainfall Asymmetry in Tropical Cyclones Making Landfall over China. *J. Appl. Meteorol. Clim.* **2014**, *54*, 117–136. [CrossRef]
24. Finocchio, P.M.; Majumdar, S.J.; Nolan, D.S.; Iskandarani, M. Idealized Tropical Cyclone Responses to the Height and Depth of Environmental Vertical Wind Shear. *Mon. Weather Rev.* **2016**, *144*, 2155–2175. [CrossRef]
25. Rios-Berrios, R.; Torn, R. Climatological Analysis of Tropical Cyclone Intensity Changes under Moderate Vertical Wind Shear. *Mon. Weather Rev.* **2017**, *145*, 1717–1738. [CrossRef]
26. Amador, J.; Alfaro, E.; Rivera, E.; Calderón, B. Climatic Features and Their Relationship with Tropical Cyclones Over the Intra-Americas Seas. In *Hurricanes and Climate Change*; Springer: Dordrecht, The Netherlands, 2010; Volume 2, pp. 149–173.
27. Deng, Y.; Gao, T.; Gao, H.; Yao, X.; Xie, L. Regional precipitation variability in East Asia related to climate and environmental factors during 1979–2012. *Sci. Rep.* **2014**, *4*, 5693. [CrossRef]
28. Guzman, O.; Jiang, H. Heavier Inner-core Rainfall of Major Hurricanes in the North Atlantic Basin than Other Global Basins. *J. Clim.* **2021**, *34*, 5707–5721. [CrossRef]
29. Stevenson, S.N.; Corbosiero, K.L.; Abarca, S.F. Lightning in Eastern North Pacific Tropical Cyclones: A Comparison to the North Atlantic. *Mon. Weather Rev.* **2015**, *144*, 225–239. [CrossRef]
30. Wu, Q.; Ruan, Z.; Chen, D.; Lian, T. Diurnal variations of tropical cyclone precipitation in the inner and outer rainbands. *J. Geophys. Res. Atmos.* **2015**, *120*, 1–11. [CrossRef]
31. Li, Y.; Cheung, K.; Chan, J.; Tokuno, M. Rainfall distribution of five landfalling tropical cyclones in the northwestern Australian region. *Aust. Meteorol. Oceanogr. J.* **2013**, *63*, 325–338. [CrossRef]
32. Cintineo, R.M.; Otkin, J.A.; Jones, T.A.; Koch, S.; Stensrud, D.J. Assimilation of Synthetic GOES-R ABI Infrared Brightness Temperatures and WSR-88D Radar Observations in a High-Resolution OSSE. *Mon. Weather Rev.* **2016**, *144*, 3159–3180. [CrossRef]
33. Lee, C.-S.; Cheung, K.; Hui, J.S.N.; Elsberry, R.L. Mesoscale Features Associated with Tropical Cyclone Formations in the Western North Pacific. *Mon. Weather Rev.* **2008**, *136*, 2006–2022. [CrossRef]
34. Hu, Y.; Zou, X. Tropical Cyclone Center Positioning Using Single Channel Microwave Satellite Observations of Brightness Temperature. *Remote Sens.* **2021**, *13*, 2466. [CrossRef]
35. Yu, Z.; Wang, Y.; Xu, H.; Davidson, N.; Chen, Y.; Chen, Y.; Yu, H. On the Relationship between Intensity and Rainfall Distribution in Tropical Cyclones Making Landfall over China. *J. Appl. Meteorol. Clim.* **2017**, *56*, 2883–2901. [CrossRef]
36. Frank, W.; Ritchie, L. Effects of Vertical Wind Shear on the Intensity and Structure of Numerically Simulated Hurricanes. *Mon. Weather Rev.* **2001**, *129*, 2249–2269. [CrossRef]
37. Corbosiero, K.; Molinari, J. The Relationship between Storm Motion, Vertical Wind Shear, and Convective Asymmetries in Tropical Cyclones. *J. Atmosph. Sci.* **2003**, *60*, 366–376. [CrossRef]
38. Kim, D.; Ho, C.-H.; Park, D.-S.R.; Kim, J. Influence of vertical wind shear on wind- and rainfall areas of tropical cyclones making landfall over South Korea. *PLoS ONE* **2019**, *14*, e0209885. [CrossRef]
39. Lemburg, A.; Bader, J.; Claussen, M. Sahel Rainfall–Tropical Easterly Jet Relationship on Synoptic to Intraseasonal Time Scales. *Mon. Weather Rev.* **2019**, *147*, 1733–1752. [CrossRef]